Subdiffraction Multicolor Imaging of the Nuclear Periphery with 3D Structured Illumination Microscopy

Lothar Schermelleh,[1]* Peter M. Carlton,[2]* Sebastian Haase,[2,4] Lin Shao,[2] Lukman Winoto,[2] Peter Kner,[2] Brian Burke,[3] M. Cristina Cardoso,[4] David A. Agard,[2] Mats G. L. Gustafsson,[5] Heinrich Leonhardt,[1]*† John W. Sedat[2]*†

Fluorescence light microscopy allows multicolor visualization of cellular components with high specificity, but its utility has until recently been constrained by the intrinsic limit of spatial resolution. We applied three-dimensional structured illumination microscopy (3D-SIM) to circumvent this limit and to study the mammalian nucleus. By simultaneously imaging chromatin, nuclear lamina, and the nuclear pore complex (NPC), we observed several features that escape detection by conventional microscopy. We could resolve single NPCs that colocalized with channels in the lamin network and peripheral heterochromatin. We could differentially localize distinct NPC components and detect double-layered invaginations of the nuclear envelope in prophase as previously seen only by electron microscopy. Multicolor 3D-SIM opens new and facile possibilities to analyze subcellular structures beyond the diffraction limit of the emitted light.

Light microscopy is a key technology in modern cell biology and, in combination with immunofluorescence, fluorescent protein fusions, or in situ hybridization, allows the specific localization of nearly all cellular components. A fundamental limitation of optical microscopy is its low resolution relative to the scale of subcellular structures. This limitation occurs because light traveling through a lens cannot be focused to a point but only to an Airy disk (*1*) with a diameter of about half the wavelength of the emitted light (*2*, *3*). Because the wavelengths of visible light range from 400 to 700 nm, objects closer than 200 to 350 nm apart cannot be resolved but appear merged into one.

Improving resolution beyond the 200-nm diffraction limit while retaining the advantages of light microscopy and the specificity of molecular imaging has been a long-standing goal. Here, we present results demonstrating that this goal can be achieved with the use of a microscope system that implements three-dimensional structured illumination microscopy (3D-SIM) (*4*) in an easy-to-use system that makes no extra demands on experimental procedures. Structured illumination microscopy (SIM) resolves objects beyond the diffraction limit by illuminating with multiple interfering beams of light (*5*). The emitted light then contains higher-resolution image information, encoded by a shift in reciprocal (Fourier, or frequency) space into observable modulations of the image, in a manner similar to the formation of Moiré patterns (fig. S1). This extra information can be decoded to reconstruct fine details, resulting in an image with twice the resolution of a conventional image taken on the same microscope (Fig. 1 and fig. S2). The 3D-SIM method extends previous 2D SIM methods by using three beams of interfering light, which generate a pattern along the axial (z) direction as well as the lateral (x and y) directions. We implemented 3D-SIM in a custom-built microscope designed for

[1]Center for Integrated Protein Science, Department of Biology, Ludwig Maximilians University Munich, 82152 Planegg-Martinsried, Germany. [2]Department of Biochemistry and Biophysics, University of California, San Francisco, CA 94143, USA. [3]Department of Anatomy and Cell Biology, University of Florida, Gainesville, FL 32610, USA. [4]Max Delbrück Center for Molecular Medicine, 13125 Berlin, Germany. [5]Department of Physiology and Program in Bioengineering, University of California, San Francisco, CA 94143, USA.

*These authors contributed equally to this work.
†To whom correspondence should be addressed. E-mail: h.leonhardt@lmu.de (H.L.); sedat@msg.ucsf.edu (J.W.S.)

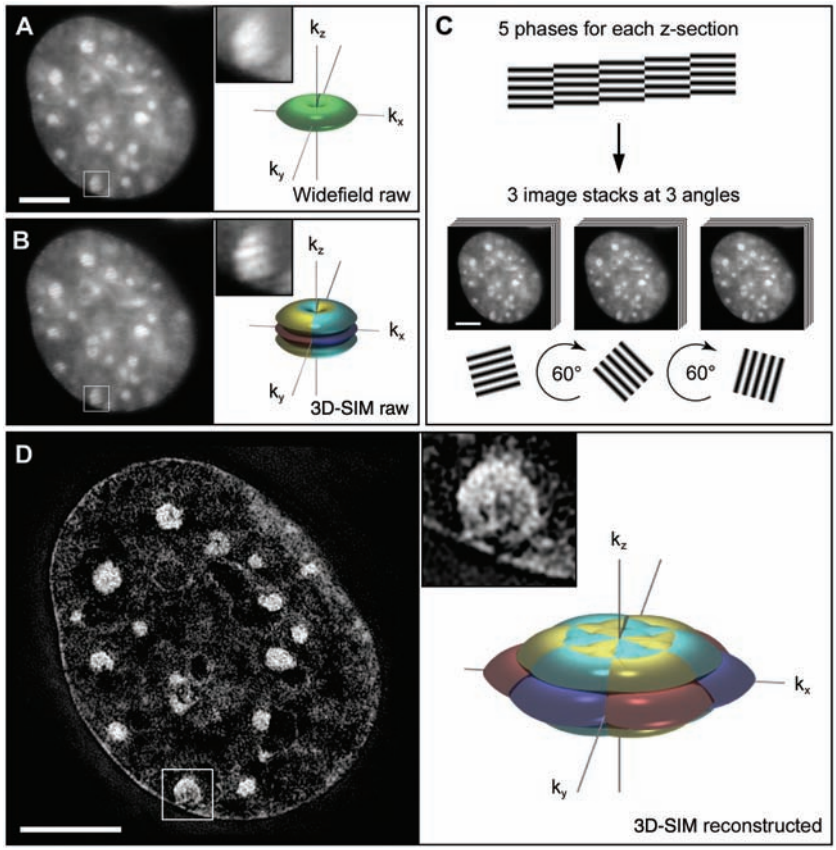

Fig. 1. Subdiffraction resolution imaging with 3D-SIM. (**A** and **B**) Cross section through a DAPI-stained C2C12 cell nucleus acquired with conventional wide-field illumination (A) and with structured illumination (B), showing the striped interference pattern (inset). The renderings to the right illustrate the respective support of detection in frequency space. The axes k_x, k_y, and k_z indicate spatial frequencies along the x, y, and z directions. The surfaces of the renderings represent the corresponding resolution limit. The depression of the frequency support ("missing cone") in z direction in (A) indicates the restriction in axial resolution of conventional wide-field microscopy. With 3D-SIM, the axial support is extended but remains within the resolution limit. (**C**) Five phases of the sine wave pattern are recorded at each z position, allowing the shifted components to be separated and returned to their proper location in frequency space. Three image stacks are recorded with the diffraction grating sequentially rotated into three positions 60° apart, resulting in nearly rotationally symmetric support over a larger region of frequency space. (**D**) The same cross section of the reconstructed 3D-SIM image shows enhanced image details compared with the original image (insets). The increase in resolution is shown in frequency space on the right, with the coverage extending two times farther from the origin. Scale bars indicate 5 μm.

ease of use so that slides prepared for conventional microscopes can be imaged without any further treatment, and operation of the microscope is similar to any modern commercial system. Although several subdiffraction-resolution optical microscopy methods have been developed in the past decade (*6*–*8*) and have been used to address specific biological questions (*9*, *10*), they still present limitations, such as the restriction of the resolution enhancement to either the lateral or the axial direction or to the near or evanescent field, limited multicolor and 3D sectioning abilities, and the requirement of unusual dyes. 3D-SIM is currently the only subdiffraction-resolution imaging technique that allows detection of three (and potentially more) wavelengths in the same sample, using standard fluorescent dyes, with 3D optical sectioning and enhancement of resolution in both lateral (x and y) and axial (z) directions.

We used 3D-SIM to probe higher-order chromatin structure and the relative localization of nuclear pores, the nuclear lamina, and chromatin at the nuclear periphery in mammalian tissue culture cells (*11*). The vertebrate nuclear pore complex (NPC) is a ~120 MD protein complex (*12*) that mediates communication and selective exchange between the nucleoplasm and cytoplasm. The relation between chromatin, the NPC, and other components of the nuclear envelope, such as the nuclear lamina, has been extensively studied (*13*, *14*). Electron microscopy (EM) has been instrumental in determining the fine structure of the NPC (*12*, *15*–*17*), but it cannot provide a global 3D view of the entire nucleus with specific labeling of the molecular components. 3D-SIM can bridge this technology gap and shed light on the nuclear periphery.

We first tested the ability of 3D-SIM to resolve the fine structure of interphase chromatin in three-dimensionally preserved formaldehyde-fixed mouse C2C12 myoblast cells stained with 4′,6-diamidino-2-phenylindole (DAPI). For comparison we recorded a reference image stack with conventional wide-field epifluorescence microscopy and applied constrained iterative deconvolution (*18*) to reduce out-of-focus blur (Fig. 2). In the 3D-SIM image, chromatin shows a more evidently fibrous substructure, and a brighter rim of heterochromatin staining is visible near the nuclear envelope as observed by EM. These chromatin-dense regions are surrounded by chromatin-poor regions, consistent with the interchromatin compartment observed by combined fluorescence and electron microscopic studies (*19*).

Unexpectedly, in 3D-SIM images of the nuclear periphery, we observed thousands of well-defined holes in DAPI staining, which could not be observed in the corresponding wide-field epifluorescence images (Fig. 2B). The size, number, and position of these holes suggested that they represented the exclusion of DNA from NPCs. To test this hypothesis and the potential of 3D-SIM for simultaneous multicolor 3D imaging of various nuclear structures, we co-immunostained these cells with NPC-specific antibodies and antibodies against lamin B. For comparison we recorded 3D image stacks of cells from the same sample with state-of-the-art confocal laser scanning microscopy (CLSM) and applied deconvolution (Fig. 3, A and B). The intermediate filament protein lamin B is a major component of the nuclear lamina that lines and stabilizes the nuclear envelope (*20*). The NPC antibodies used here (referred to as αNPC) are directed against the FG-repeat domain common to several nuclear pore proteins and mainly detect Nup62, Nup214, and Nup358, which are located in the center and at the cytoplasmic side of the NPC (*21*) with a minor signal from Nup153. In lateral cross sections of 3D-SIM image stacks, we consistently observed the peripheral heterochromatin rim outlined by a fine heterogeneous layer of the nuclear lamina and nuclear pore signals further above the lamina. This clear triple-layered organization was not resolvable with CLSM (Fig. 3A). For comparison, we also used a monoclonal antibody specific for Nup153, which is located on the nucleoplasmic side of the NPC (*21*) and obtained a pore signal in the same plane as the lamin B signal, demonstrating the potential of 3D-SIM to resolve subtle differences of epitope locations within the NPC (Fig. 3C). In apical cross sections, we found that NPC foci strictly localize within DAPI voids (Fig. 3B and movie S1). With very few exceptions, every DAPI void contained a focus of NPC staining and vice versa, suggesting that most if not all NPCs exclude chromatin from their immediate vicinity.

We calculated the density of NPC foci in 3D-SIM and confocal images (Fig. 3 and fig. S3) by using automatic detection with identical criteria.

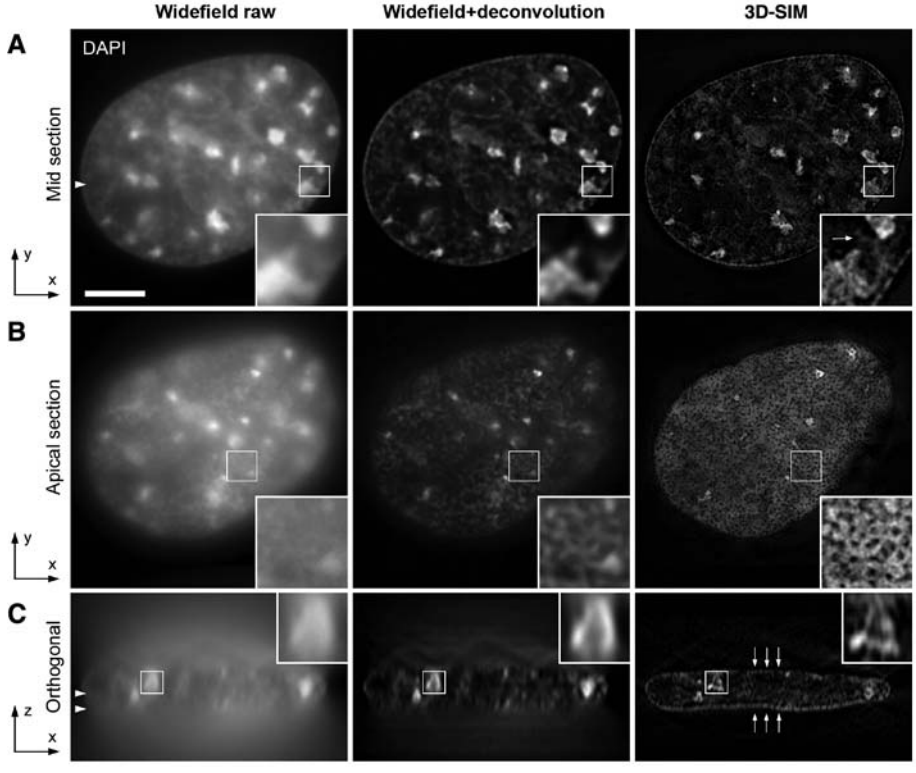

Fig. 2. Comparison of wide-field imaging and 3D-SIM in resolving interphase chromatin fine structure. 3D image stacks of the same DAPI-stained C2C12 cell nucleus were recorded with conventional wide-field illumination (left) and with 3D-SIM (right). Deconvolution was applied to the wide-field data set (middle). Scale bar, 5 μm. Arrowheads indicate the position of the respective cutting planes. (**A**) Mid cross section shows brightly stained chromocenters of clustered (peri-)centromeric heterochromatin. (Insets) Higher-detail information of chromatin substructures when recorded with 3D-SIM. Arrow points to a less-bright chromatin structure that has been spuriously eroded by the deconvolution procedure. (**B**) Projection of four apical sections (corresponding to a thickness of 0.5 μm) taken from the surface of the nuclear envelope closest to the coverslip. Whereas the raw image shows diffuse DAPI staining, the deconvolved image shows more pronounced variations in fluorescence intensities. Image data with 3D-SIM extended-resolution information reveal a punctuated pattern of regions devoid of DAPI staining. (**C**) Orthogonal cross-section through the entire 3D image stack demonstrates the low sectioning capability of conventional wide-field microscopy, which cannot be mitigated solely by deconvolution. In contrast, clear layers of peripheral heterochromatin can be resolved with 3D-SIM (arrows).

The 3D-SIM image showed an average (±SD) of 5.6 ± 3.3 foci per μm^2, whereas only 2.8 ± 1.1 foci per μm^2 were detected in the confocal image. By comparison, 12 ± 1.8 NPCs per μm^2 have been observed in mouse liver nuclei by freeze-fracture EM (*22*). Although the numbers cannot be directly compared because of cell type and cell cycle–dependent variations (*23*), they still indicate that 3D-SIM detects and resolves most NPCs and outperforms CLSM.

Although the discrete chromatin voids at NPCs are not visible in confocal or standard wide-field images, the intensity of DAPI staining should still show fluctuations that anticorrelate with NPC foci. We also reasoned that, even though the lamina does not show a striking one-to-one exclusion from NPCs under any of our methods, it should still be anticorrelated with the NPCs. To pursue these questions, we examined the average environment of an NPC focus in our images (fig. S4). Sub-images were cropped from the data set centered on the peak intensities of NPC foci, which were automatically detected in 3D. Intensity profiles through the center of each sub-image show a drop in intensity in DAPI staining, centered on the NPC focus, in all confocal and 3D-SIM images. A similar drop in intensity of the lamin signal is seen only in the case of 3D-SIM. In composites of the sub-images, a central hole can be seen in the DAPI channel. This indicates that the expected intensity fluctuations are present in all cases. The composite lamina image recorded by 3D-SIM also shows a hole, which was not detected by confocal microscopy. The width of the NPC signal was determined from intensity profiles by measuring the full width at half maximum. With CLSM this width was ~200 nm (192 ± 17 and 192 ± 11 nm before and after deconvolution, respectively), which essentially reflects the point spread function (PSF) of CLSM. In contrast, the measured width of NPC signal recorded with 3D-SIM was 120 ± 3 nm, which is in good agreement with EM measurements (*15*).

Many of the nuclei we imaged contained invaginations of the nuclear envelope that are especially prominent near the centrosome during prophase. These invaginations have been shown by EM studies to be tubular extensions of both nuclear envelopes (*24*), but because their width is generally smaller than the diffraction limit they appear as a single line by conventional microscopy. We investigated these nuclear invaginations in prophase nuclei by CLSM and 3D-SIM (Fig. 4) and could resolve the bilaminar structure of these invagination only with 3D-SIM (movie S2). This detailed substructure of nuclear

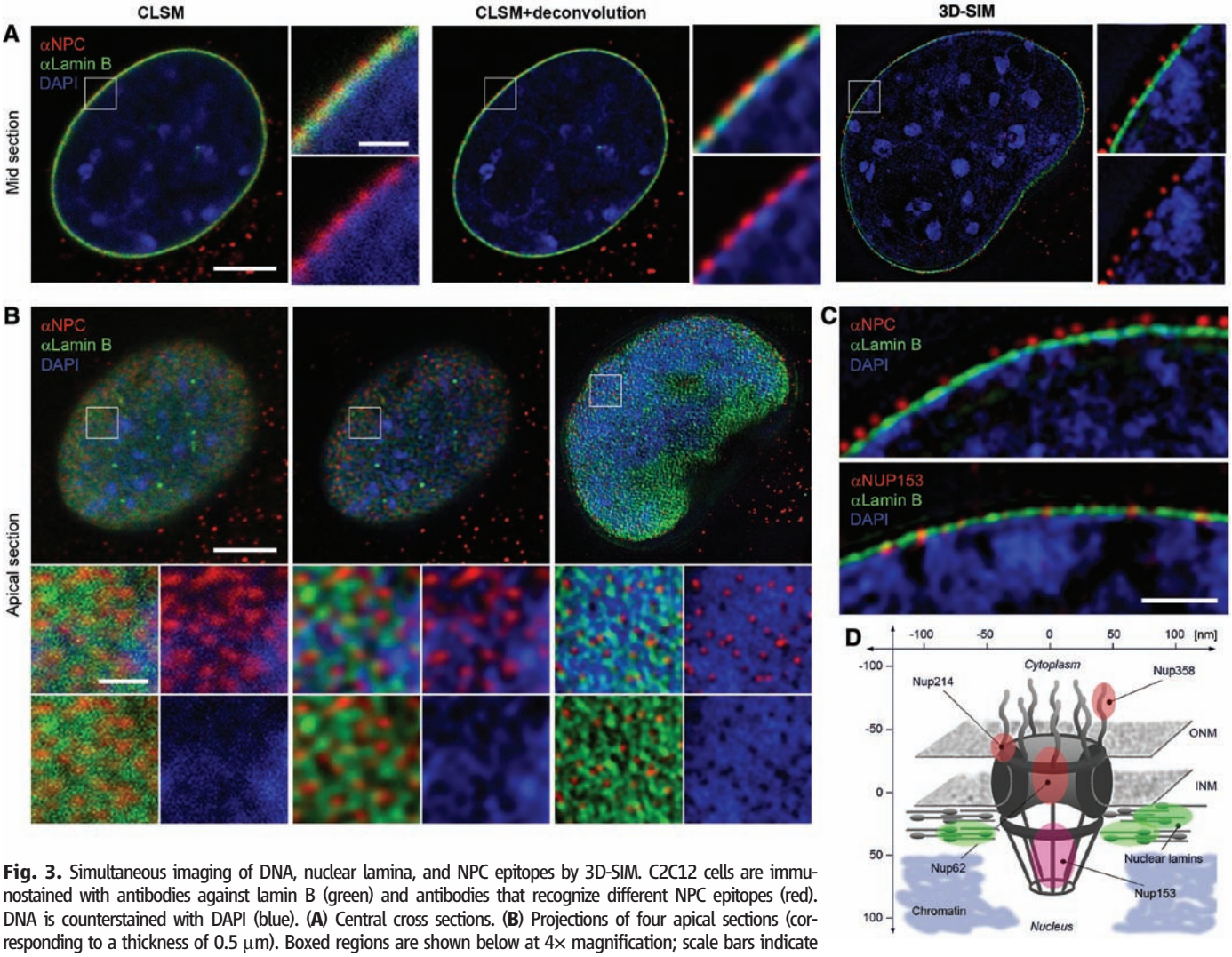

Fig. 3. Simultaneous imaging of DNA, nuclear lamina, and NPC epitopes by 3D-SIM. C2C12 cells are immunostained with antibodies against lamin B (green) and antibodies that recognize different NPC epitopes (red). DNA is counterstained with DAPI (blue). (**A**) Central cross sections. (**B**) Projections of four apical sections (corresponding to a thickness of 0.5 μm). Boxed regions are shown below at 4× magnification; scale bars indicate 5 μm and 1 μm, respectively. (A) CLSM and deconvolution still show partially overlapping signals. In contrast, with 3D-SIM the spatial separation of NPC, lamina, and chromatin and chromatin-free channels underneath nuclear pores are clearly visible. (B) Top view on the nuclear envelope. Whereas CLSM fails to resolve close nuclear pores, 3D-SIM shows clearly separated NPC signals at voids of peripheral chromatin and surrounded by an irregular network of nuclear lamina. (**C**) Mid sections comparing stainings with an antibody that mainly reacts with Nup214, Nup358, and Nup62 (αNPC) and one specifically recognizing Nup153 (αNup153). The αNPC signal is above the lamina (140 ± 8 nm), whereas the αNup153 pore signal is at the same level as the lamina (–15 ± 20 nm). Scale bars 1 μm. (**D**) Schematic outline of the NPC, showing the relative position of Nup proteins and surrounding structures. ONM, outer nuclear membrane; INM, inner nuclear membrane.

invaginations has so far only been detected by transmission electron microscopy (TEM) (fig. S5). We also quantified the width of the lamin B signal in interphase nuclei in lateral and axial directions by fitting Gaussian curves to the measured intensities. Because the thickness of the lamina is in the range of 20 to 50 nm, the obtained values should reflect the resolution limit of either of the applied methods. With 3D-SIM we determined a width of threads in the lamin network with an upper limit of 98 ± 12 nm laterally and 299 ± 22 nm axially, whereas confocal images showed more than twofold higher values (243 ± 30 nm laterally and 736 ± 225 nm axially). Subsequent deconvolution of CLSM data/images did not improve the lateral (231 ± 28 nm) but did improve the axial (418 ± 26 nm) resolution, which is mostly due to an increased signal-to-noise ratio by removing out-of-focus blur and suppression of background (*2*). This 3D imaging of complex biological structures demonstrates about twofold enhanced resolution of 3D-SIM over conventional fluorescence imaging techniques in lateral and axial directions.

Many cellular structures and macromolecular complexes, including the nuclear envelope and its pores, fall just below the diffraction limit of conventional light microscopy, preventing quantitative analysis. In doubling the resolution of conventional microscopy in three dimensions, 3D-SIM was able to resolve individual nuclear pores, detect and measure the exclusion of chromatin and the nuclear lamina from nuclear pores, and accurately image invaginations of the nuclear envelope caused by the formation of the mitotic spindle. We have demonstrated both an increase in quantitative precision of measurement and the detection of novel cytological features, by imaging to a resolution approaching 100 nm. Although this level of resolution is less than that afforded by other techniques such as stimulated emission depletion (STED), photoactivated localization (PALM), or stochastic optical reconstruction (STORM) microscopy (*25*–*29*), 3D-SIM is currently the only subdiffraction-resolution imaging technique that can produce multicolor 3D images of whole cells with enhancement of resolution in both lateral and axial directions. Notably, these results were obtained with standard cytological methods, without the need for unconventional fluorescent dyes or coverslips, and on a microscope platform designed to be no more difficult to use than a conventional commercial microscope. The possibility of using 3D-SIM with well-established standard labeling techniques and to simultaneously locate different molecules or structures in the 3D cellular context opens interesting new perspectives for molecular cell biology.

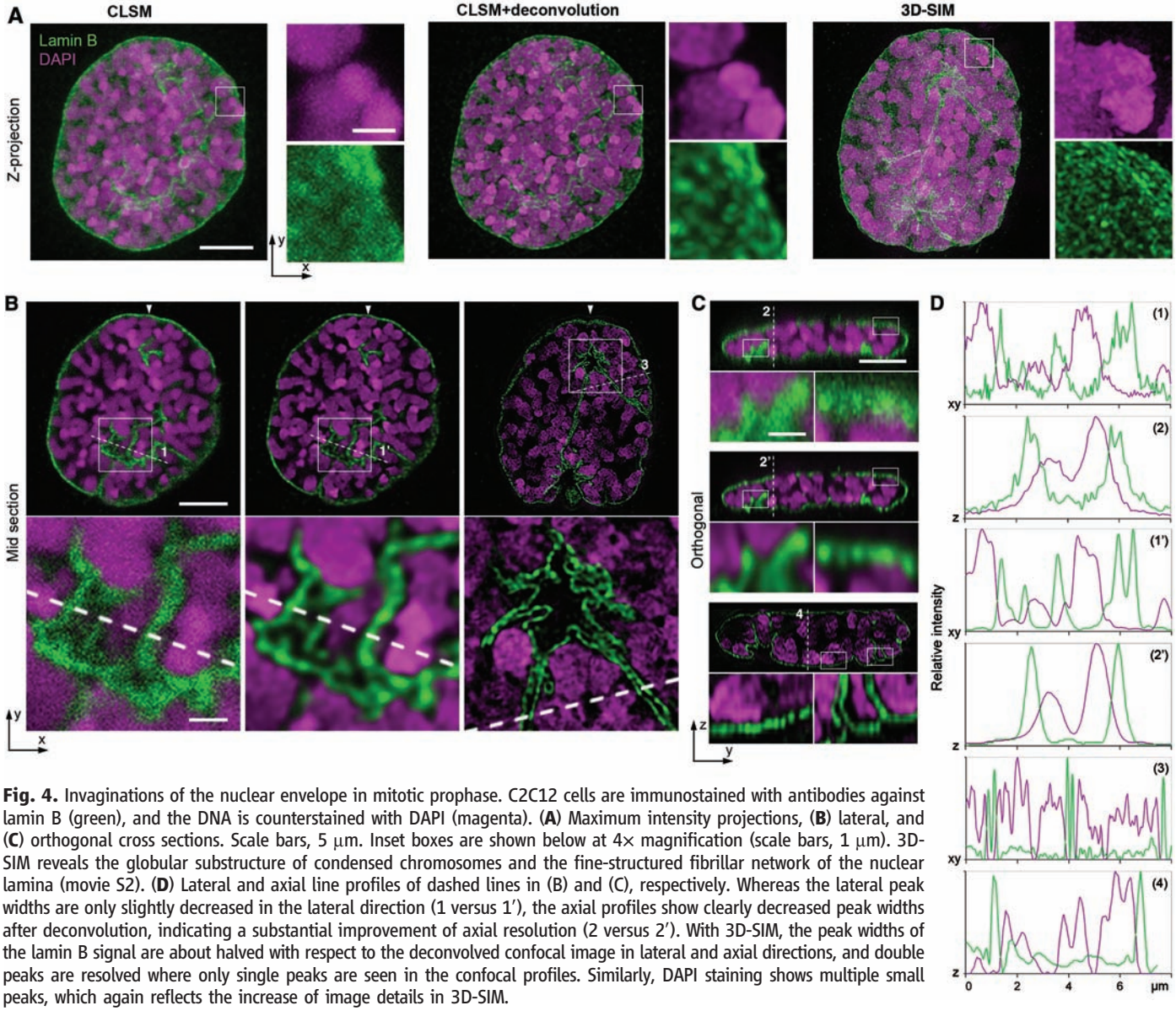

Fig. 4. Invaginations of the nuclear envelope in mitotic prophase. C2C12 cells are immunostained with antibodies against lamin B (green), and the DNA is counterstained with DAPI (magenta). (**A**) Maximum intensity projections, (**B**) lateral, and (**C**) orthogonal cross sections. Scale bars, 5 μm. Inset boxes are shown below at 4× magnification (scale bars, 1 μm). 3D-SIM reveals the globular substructure of condensed chromosomes and the fine-structured fibrillar network of the nuclear lamina (movie S2). (**D**) Lateral and axial line profiles of dashed lines in (B) and (C), respectively. Whereas the lateral peak widths are only slightly decreased in the lateral direction (1 versus 1′), the axial profiles show clearly decreased peak widths after deconvolution, indicating a substantial improvement of axial resolution (2 versus 2′). With 3D-SIM, the peak widths of the lamin B signal are about halved with respect to the deconvolved confocal image in lateral and axial directions, and double peaks are resolved where only single peaks are seen in the confocal profiles. Similarly, DAPI staining shows multiple small peaks, which again reflects the increase of image details in 3D-SIM.

References and Notes

1. M. Born, E. Wolf, Eds., *Principle of Optics* (Cambridge Univ. Press, Cambridge, 1998).
2. J. B. Pawley, Ed., *Handbook of Biological Confocal Microscopy* (Springer, New York, ed. 3, 2006).
3. E. Abbe, *Arch. Mikrosk. Anat.* **9**, 413 (1873).
4. M. G. Gustafsson *et al.*, *Biophys. J.*, in press; published online 7 March 2008 (10.1529/biophysj.107.120345).
5. M. G. Gustafsson, *J. Microsc.* **198**, 82 (2000).
6. R. Heintzmann, G. Ficz, *Brief. Funct. Genomics Proteomics* **5**, 289 (2006).
7. S. W. Hell, *Nat. Biotechnol.* **21**, 1347 (2003).
8. S. W. Hell, *Science* **316**, 1153 (2007).
9. R. J. Kittel *et al.*, *Science* **312**, 1051 (2006); published online 13 April 2006 (10.1126/science.1126308).
10. K. I. Willig, S. O. Rizzoli, V. Westphal, R. Jahn, S. W. Hell, *Nature* **440**, 935 (2006).
11. Material and methods are available on *Science* Online.
12. R. Reichelt *et al.*, *J. Cell Biol.* **110**, 883 (1990).
13. B. Burke, C. L. Stewart, *Nat. Rev. Mol. Cell Biol.* **3**, 575 (2002).
14. M. R. Paddy, A. S. Belmont, H. Saumweber, D. A. Agard, J. W. Sedat, *Cell* **62**, 89 (1990).
15. M. Beck *et al.*, *Science* **306**, 1387 (2004); published online 28 October 2004 (10.1126/science.1104808).
16. M. Beck, V. Lucic, F. Forster, W. Baumeister, O. Medalia, *Nature* **449**, 611 (2007).
17. D. Stoffler *et al.*, *J. Mol. Biol.* **328**, 119 (2003).
18. D. A. Agard, Y. Hiraoka, P. Shaw, J. W. Sedat, *Methods Cell Biol.* **30**, 353 (1989).
19. H. Albiez *et al.*, *Chromosome Res.* **14**, 707 (2006).
20. L. Gerace, A. Blum, G. Blobel, *J. Cell Biol.* **79**, 546 (1978).
21. B. Fahrenkrog *et al.*, *J. Struct. Biol.* **140**, 254 (2002).
22. R. Tonini, F. Grohovaz, C. A. Laporta, M. Mazzanti, *FASEB J.* **13**, 1395 (1999).
23. M. Winey, D. Yarar, T. H. Giddings Jr., D. N. Mastronarde, *Mol. Biol. Cell* **8**, 2119 (1997).
24. M. Fricker, M. Hollinshead, N. White, D. Vaux, *J. Cell Biol.* **136**, 531 (1997).
25. M. Bates, B. Huang, G. T. Dempsey, X. Zhuang, *Science* **317**, 1749 (2007); published online 15 August 2007 (10.1126/science.1146598).
26. E. Betzig *et al.*, *Science* **313**, 1642 (2006); published online 9 August 2006 (10.1126/science.1127344).
27. G. Donnert *et al.*, *Proc. Natl. Acad. Sci. U.S.A.* **103**, 11440 (2006).
28. B. Huang, W. Wang, M. Bates, X. Zhuang, *Science* **319**, 810 (2008); published online 2 January 2008 (10.1126/science.1153529).
29. M. J. Rust, M. Bates, X. Zhuang, *Nat. Methods* **3**, 793 (2006).

30. This work was supported by grants from the Bavaria California Technology Center, the Center for NanoScience, the Nanosystems Initiative Munich, and the Deutsche Forschungsgemeinschaft to L. Schermelleh, M.C.C., and H.L.; by NIH grant GM-2501–25 to J.W.S.; by the David and Lucile Packard Foundation; and by NSF through the Center for Biophotonics, an NSF Science and Technology Center managed by the University of California, Davis, under cooperative agreement no. PHY 0120999. P.M.C. is partially supported by the Keck Laboratory for Advanced Microscopy at the University of California, San Francisco. We thank A. Čopič, K. Weis, and F. Spada for comments on the manuscript and helpful discussions. P.M.C., L. Shao, L.W., and P.K. have performed limited paid consulting for Applied Precision, which is planning a commercial microscope system using three-dimensional structured illumination. The University of California holds patents for structured illumination microscopy.

Supporting Online Material

www.sciencemag.org/cgi/content/full/320/5881/1332/DC1
Materials and Methods
Figs. S1 to S6
References and Notes
Movies S1 and S2

25 February 2008; accepted 13 May 2008
10.1126/science.1156947

Intersection of the RNA Interference and X-Inactivation Pathways

Yuya Ogawa, Bryan K. Sun, Jeannie T. Lee*

In mammals, dosage compensation is achieved by X-chromosome inactivation (XCI) in the female. The noncoding *Xist* gene initiates silencing of the X chromosome, whereas its antisense partner *Tsix* blocks silencing. The complementarity of Xist and Tsix RNAs has long suggested a role for RNA interference (RNAi). Here, we report that murine Xist and Tsix form duplexes in vivo. During XCI, the duplexes are processed to small RNAs (sRNAs), most likely on the active X (Xa) in a Dicer-dependent manner. Deleting *Dicer* compromises sRNA production and derepresses *Xist.* Furthermore, without Dicer, Xist RNA cannot accumulate and histone 3 lysine 27 trimethylation is blocked on the inactive X (Xi). The defects are partially rescued by truncating Tsix. Thus, XCI and RNAi intersect, down-regulating *Xist* on Xa and spreading silencing on Xi.

X-chromosome inactivation (XCI) (*1*) balances X-chromosome dosages between XX and XY individuals. XCI is initiated by *Xist* (*2*, *3*) and opposed by *Tsix* (*4*). How *Xist* induces XCI on inactive X (Xi) and how *Tsix* stably silences *Xist* on active X (Xa) remain two unanswered questions. A role for RNA interference (RNAi) has long been speculated. RNAi refers to the repressive influence of double-stranded RNA (dsRNA) on gene transcription and transcript stability (*5*, *6*). Numerous similarities, including the involvement of noncoding RNAs, can be found between XCI and RNAi silencing of constitutive heterochromatin. However, a deficiency of Dicer (Dcr) has no obvious effect on maintaining Xi in T cells (*7*) and, although Xist and Tsix RNAs are perfectly complementary, dsRNAs had never been observed in vivo.

Here, we formally explore a role for RNAi in XCI. To search for small RNAs (sRNAs) within *Xist/Tsix*, we performed Northern analysis in mouse embryonic stem (ES) cells, a model that recapitulates XCI during cell differentiation ex vivo; and in mouse embryonic fibroblasts (MEFs), post-XCI cells that faithfully maintain one Xi. At repeat A, a region of *Xist* required for silencing (*8*), we observed sRNAs at ~30 nucleotides (nt) and ~37 nt in the Tsix orientation and at ~25 and ~35 nt in the Xist orientation (Fig. 1A). At *Xist* exon 7, sRNAs occurred between 24 and 42 nt on the Tsix strand and at ~25 and ~35 nt on the Xist strand (Fig. 1B). At the promoter, robust quantities of Tsix-strand sRNAs were observed (Fig. 1C). sRNAs were also seen on the Xist strand, implying that low-level sense transcription must occur at the promoter. The integrity of all Northern blots was confirmed by micro RNA 292-as (miRNA292-as) and tRNA controls (Fig. 1 and fig. S1). The sRNAs were developmentally regulated, being unmeasurable in the pre-XCI [day 0 (d0)] and post-XCI (MEF) states and detectable only during XCI (d4 and d10). Furthermore, sRNAs occurred in both XX and XY cells. For discussion purposes, we call them xiRNA for their X-inactivation center origin, distinct from the smaller small interfering RNA (siRNAs) and miRNAs.

To determine whether xiRNA production depends on antisense expression, we investigated ES cells in which *Tsix* was deleted ($Tsix^{\Delta CpG}$) (*4*) and the *Tsix* regulator *Xite* ($Xite^{\Delta L}$) (*9*). Deleting *Tsix* resulted in a dramatic reduction in antisense-strand xiRNA (Fig. 1D). A residual level of xiRNA was still detectable, consistent with cryptic promoter activity in $Tsix^{\Delta CpG}$ (*4*). Deleting *Xite* likewise reduced antisense xiRNA levels, consistent with a requirement for *Xite* in transactivating *Tsix* (*9*). In the sense orientation, both deletions also compromised xiRNA production. Thus, sRNAs are indeed generated from *Xist/Tsix* and depend on *Tsix* and *Xite* expression.

The presence of xiRNAs implied that Tsix and Xist must exist as long duplex precursors. However, the developmental timing of xiRNA appearance is paradoxical: Although Tsix and Xist are biallelically expressed on d0, they become monoallelically expressed on opposite Xs during XCI (*4*). On d0, three to five copies per chromosome of Xist RNA are present, whereas Tsix occurs at >10-fold molar excess (*10*–*12*). Upon XCI, Tsix is down-regulated on Xi as Xist up-regulates >30-fold. On Xa, Tsix persists as Xist is down-regulated. How would dsRNA form when Tsix and Xist, both cis-limited, are on opposite chromosomes during XCI?

Department of Molecular Biology, Massachusetts General Hospital; Department of Genetics, Harvard Medical School; and Howard Hughes Medical Institute, Boston, MA 02114, USA.

*To whom correspondence should be addressed. E-mail: lee@molbio.mgh.harvard.edu

Supporting Online Material for

Subdiffraction Multicolor Imaging of the Nuclear Periphery with 3D Structured Illumination Microscopy

Lothar Schermelleh, Peter M. Carlton, Sebastian Haase, Lin Shao, Lukman Winoto, Peter Kner, Brian Burke, M. Cristina Cardoso, David A. Agard, Mats G. L. Gustafsson, Heinrich Leonhardt,* John W. Sedat*

*To whom correspondence should be addressed. E-mail: h.leonhardt@lmu.de (H.L.); sedat@msg.ucsf.edu (J.W.S.)

Published 6 June 2008, *Science* **320**, 1332 (2008)
DOI: 10.1126/science.1156947

This PDF file includes:

Other Supporting Online Material for this manuscript includes the following:
available at www.sciencemag.org/cgi/content/full/320/5881/1332/DC1

Supporting online material

Materials and Methods

The 3dSIM microscope (OMX)

We designed and constructed a custom microscope platform for the purpose of implementing advanced optical technologies, including superresolution (3dSIM) and fast live three-dimensional imaging, in a facile, user-friendly system. The entire microscope platform, named "OMX" (**O**ptical **M**icroscope, e**X**perimental) is a radical redesign. For 3dSIM, solid-state or diode laser illumination is coupled into a multi-mode fiberoptic cable and passed through a diffraction grating. The grating is mounted on a high-precision piezoelectric stage (Piezosystems Jena) which provides phase control of the pattern by translation into five positions. The piezoelectric stage is itself mounted on a rotational stage which orients the grating into the three different angular orientations required. The piezoelectric stage is feedback controlled from a capacitive position sensor acting against a fixed cylindrical counter-electrode, which allows the pattern phase to be controlled precisely without being affected by any drift in the piezo-actuator or instability in the rotation stage bearings. A set of lenses and mirrors placed on a modular "zoom plate" focuses the diffracted beams to single points in the back focal plane of the objective. Different zoom plates can be substituted to optimize the beam separation in the objective pupil for the longest excitation wavelength to be used in a given experiment. Similar flexibility could alternatively be supplied by making the grating exchangable. A beam blocker is placed before the objective and adjusted to block all but the innermost three beams (orders -1, 0, and 1). The objective used was plan-apochromatic 100x, 1.4 NA, oil-immersion (Olympus), and was mounted in a plate made of zerodur, a ceramic with a very low thermal expansion coefficient (~ 0.10 x 10^{-6}/K). Immersion oil of refractive index 1.1515 was used, after being empirically determined to give the most symmetric point spread function (data not shown). The sample is mounted on a slide-holder also made of zerodur, which is

connected to a second piezoelectric stage (Piezosystems Jena) providing translation in z of ±30 µm. This piezoelectric stage is in turn mounted on a stage with Nanomover motion (Applied Precision) which provides a wider range of positioning. Emitted light from the sample passes through a set of four dichroic mirrors, which direct light of different wavelengths into four independently controlled cameras; thus, four wavelengths can be recorded simultaneously (Fig. S6). This setup, in which emitted light is reflected rather than transmitted through filters, is unique to OMX and is designed to maximize detection sensitivity. Images are acquired with iXon 87 back-illuminated EMCCD cameras, with 512 x 512 pixels with >90% quantum efficiency (Andor Technology). All operations of the microscope are controlled by custom-written software in C++ and Python. One main control program on a dedicated computer operates subprograms on six remote computers (one for each of the four cameras; one for the Nanomover, and one for the digital signal processor used to achieve sub-millisecond precision in the timing of image acquisition, shutters, and stage motion.

3dSIM image acquisition

Light from one of three lasers (405 nm, 488 nm, or 532 nm) is coherence-scrambled by a holographic diffuser before being coupled through a multimode fiberoptic cable and collimated onto a custom fused silica linear transmission grating. The grating splits the incident light into multiple orders, the innermost three of which (orders 0, +1, and -1) interfere in the image plane to produce a three-dimensional stripe pattern with a lateral line spacing of approximately 0.2 µm. The pattern was made to illuminate sequential planes (z-sections) of the sample by moving the stage in the z-direction with a step size of 0.125 µm. For each z-section, 5 phases of the sinusoidal pattern were recorded sequentially by translating the diffraction grating between exposures. Three z-stacks are recorded one after the other in this manner with three angular orientations of the diffraction grating, 60° apart. Exposure times were between 100-500 ms, yielding typically 1,000 to 10,000 counts in a raw image of 16-bit dynamic range. A 300 ms pause

was added between each exposure, as such pausing was empirically observed to decrease photobleaching. For multi-color fluorescence experiments, the color channels were recorded sequentially onto separate CCD cameras. Alignment of color channels was performed by custom Python scripts applying translation, rotation, and both isotropic and anisotropic scaling, using alignment parameters obtained from measurements with 100 nm multi-wavelength fluorescent beads (Molecular Probes) taken with the same camera setup as the biological samples.

Image processing

Raw images were saved to disk and processed to reconstruct high-resolution information (*1*). For automatic point finding, the FindPoints program in the Priism suite (*2*) was used; points were located by finding local maxima in regions containing pixel intensities five standard deviations higher than the mean intensity. Analysis of sub-regions centered on detected points was performed with GNU Octave, version 2.1.71. The distance of nuclear pore signals from the nuclear lamina was calculated by fitting a 2^{nd} order polynomial curve to image pixels above a threshold, and taking the average distance between the curves.

Cell culture and immunofluorescence staining

Mouse C2C12 myoblasts were cultured in DMEM supplemented with 20% FBS and 50 µg/ml gentamycin. Cells were grown to 60-80% confluency on 18x18 mm cover glasses and fixed with 3.7% formaldehyde (Sigma) in PBS. All washing steps after fixation were performed with 0.02% Tween in PBS (PBST). Cells were permeabilized with 0.5% Triton X-100 in PBS. Primary antibodies used were: goat polyclonal anti-Lamin B (C-20, Santa Cruz), mouse monoclonal anti-NUP153 and a mouse monoclonal anti-NPC that mainly reacts with Nup62, Nup214 and Nup358 with only a relatively minor signal from Nup153 (sold as “anti-NUP153”, QE5, Abcam). Secondary antibodies (Molecular Probes) were coupled to Alexa488 for green fluorescence and Alexa555 or Alexa568 for red fluorescence. All secondary antibodies were highly cross adsorbed to avoid cross-reaction. In most cases, cells

were postfixed with 3.7% formaldehyde in PBS after incubation with secondary antibodies and washing in order to minimize background fluorescence and floating particles or precipitates. After additional washing steps cells were counterstained with 100 ng/ml DAPI in PBST for 5 min. Cells were mounted on microscope slides with Vectashield mounting medium (Vector Laboratories).

Confocal laser scanning microscopy

Confocal image stacks were recorded with a TCS SP2 AOBS confocal laser scanning microscope (Leica) using a 63x/1.4 NA HXA Plan-Apochromat oil immersion objective. Fluorochromes were excited with a 405 nm diode laser, the 488 nm line of an argon laser and a 561 nm diode-pumped solid state (DPSS) laser. Settings used were: 512x512 pixels frame size; 40 or 50 nm pixel size, 125 nm z-distances between sections; 1 Airy Unit pinhole diameter; 800 Hz scan speed; 6-times averaging. Deconvolution of confocal datasets was performed with Huygens software (SVI) using measured point spread functions and maximum-likelihood-estimation algorithm (settings: signal-to-noise: 15, maximum iterations: 40, quality criterion 0.1). For presentation, we used linear contrast enhancement on entire images. For 2-color figures we chose magenta as a false color for red fluorescence, to accommodate for colorblindness.

Supporting figures

Fig. S1. Moiré pattern formation at macroscopic scale. The interference between two fine non-resolvable patterns (flanking arrowheads) creates a coarser, resolvable Moiré pattern (center arrow). This pattern resembles and contains structural information about the underlying non-resolvable structure as demonstrated by the close-up view (inset) of the boxed region.

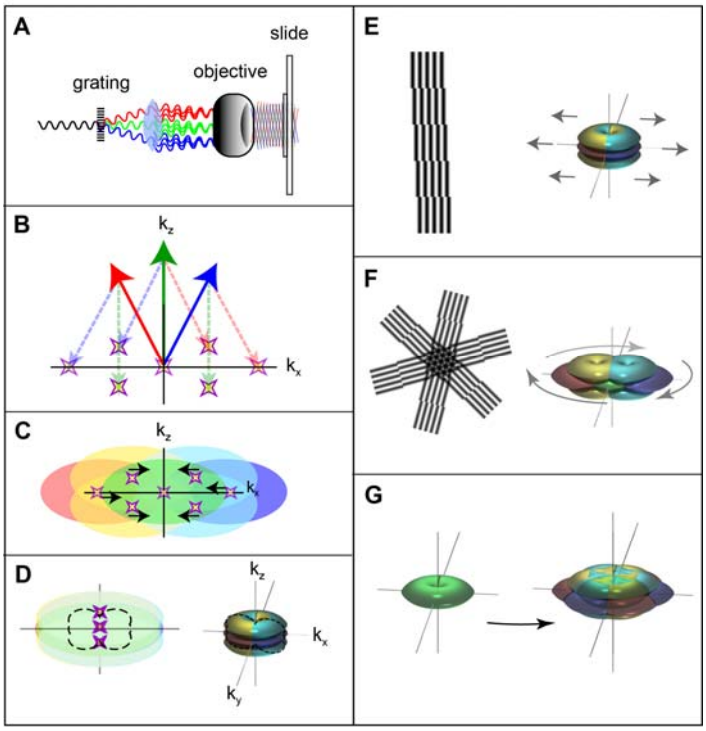

Fig. S2. Outline of the 3D-SIM method. (Throughout this figure, color is used for clarity only, and does not indicate wavelength.) (**A**) Incident light is diffracted by a grating into multiple orders, the innermost three of which are focused at the back focal plane of the objective. These three beams, each re-collimated by the objective, intersect and interfere in the sample plane, producing the 3D structured illumination pattern. (**B–G**) A representation of structured illumination in Fourier space. Axis k_x, k_y, and k_z indicates spatial frequency in x, y and z direction, respectively. (**B**) Amplitude wave vectors of the incident light beams are represented by colored vectors. Spatial frequencies in the illumination intensity (stars), corresponding to pairwise interference of these three beams, occur at the pairwise differences of these amplitude vectors. These difference vectors are here constructed by adding the negative of each vector to the others (dashed lines). (**C**) The moiré effect results in the lateral shifting of sample information toward the k_z axis by vectors corresponding to each illumination intensity component (starred positions). This brings information from normally unobservable regions of frequency space into the observable region of the microscope. There are five

shifts, color-coded red, yellow, green, cyan, and blue; the observed image is the sum of all five. For clarity, these are here illustrated with ellipses; the actual shape of the region made observable by each component is rendered in panel (F). The observable region for the intermediate-lateral-frequency information components (yellow and light blue) is extended axially according to the axial position of the corresponding illumination intensity components; this phenomenon is explained in reference (4) of the main text. (**D**) The frequency content of the raw data is indicated by the dashed line, shown in 2D cross-section (left) and rendered in 3D (right). (**E**) Five images with different phase settings of the diffraction grating are acquired at each z-section, in order to have five linearly independent linear combinatons of the five shifted components. Since the number of equations equals the number of unknowns, the contribution of each component can be calculated and separated from the others. Then each component is computationally shifted laterally away from the origin to its true position, extending frequency-space coverage in one lateral direction. (**F**) To cover all directions, the procedure is repeated for two more orientations of the pattern. (**G**) Comparison of the coverage in frequency space: left, conventional widefield microscopy; right, 3D-SIM. Notably, the "missing cone" of information that plagues conventional microscopy has been filled in, and both axial and lateral resolution have increased by a factor of two. For a more detailed description of the method, see reference *S1*.

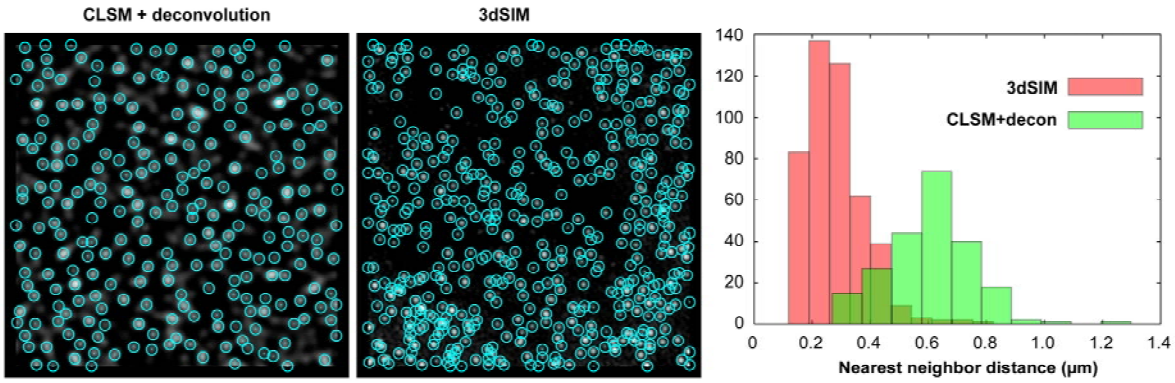

Fig. S3. Density of Nuclear Pores. (**A**) 10 µm^2 subsets of nuclei from Fig. 3 are shown, with detected nuclear pores circled. (**B**) Histograms of nearest-neighbor distances are shown. The mean nearest-neighbor distance of NPC foci in the 3dSIM image is 251 nm and 440 nm in the confocal image.

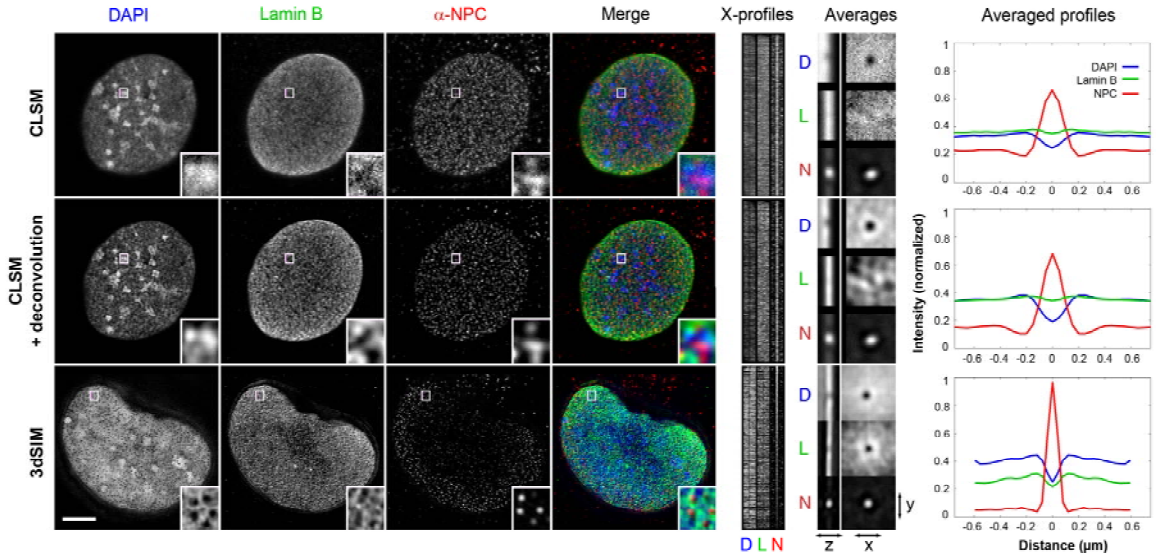

Fig. S4. Comparison of NPC environments between microscopy methods. Images of C2C12 nuclei are shown as 1 µm maximum-intensity projections from the surface of the nucleus closest to the coverslip. Rows 1 and 2 show confocal image data of the same nucleus before and after deconvolution. Scale bar, 5 µm. Insets are shown at 5x magnification. In the merged color image, DAPI is shown in blue, anti-Lamin B staining in green, and anti-NPC staining in red. *X-profiles* display vertically aligned line scans through 420 separate NPC foci (the number of foci detected in the raw confocal image; other channels contained more foci, but only a randomly chosen subset of 420 was analyzed. NPC foci were automatically segmented and placed in the centers of 3D matrices containing 31 x 31 x 13 elements. The profile lines shown are drawn through the position of the peak intensity pixel of the NPC in x-direction in each channel. The center vertical line through the NPC channel shows the bright NPC focus detected in that channel; dark lines through other channels demonstrate the lack of DAPI and Lamin B signals in the same region. *Averages* display 3D matrices containing the 420 foci intensity-normalized and averaged together. Rows labeled D (DAPI), L (Lamin B) and N (NPC) continue in the same sequence in each case. The left column shows slices through the yz-plane centered on the NPC focus for each channel, while the

right column shows slices through the xy-plane. Averaged profiles display intensity plots through radially averaged 3D images at left. Intensities were normalized between 0 and 1 and plotted through the xy-diagonal of the z-section containing the brightest NPC intensity.

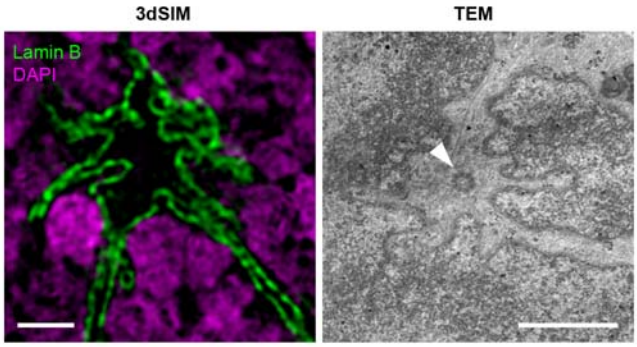

Fig S5. Comparison of a prophase invagination of the nuclear envelope imaged with 3dSIM and with transmission electron microscopy (TEM). The arrowhead indicates a centriole with emanating microtubules surrounded by invaginations of the nuclear membrane. Bars, 1 µm.

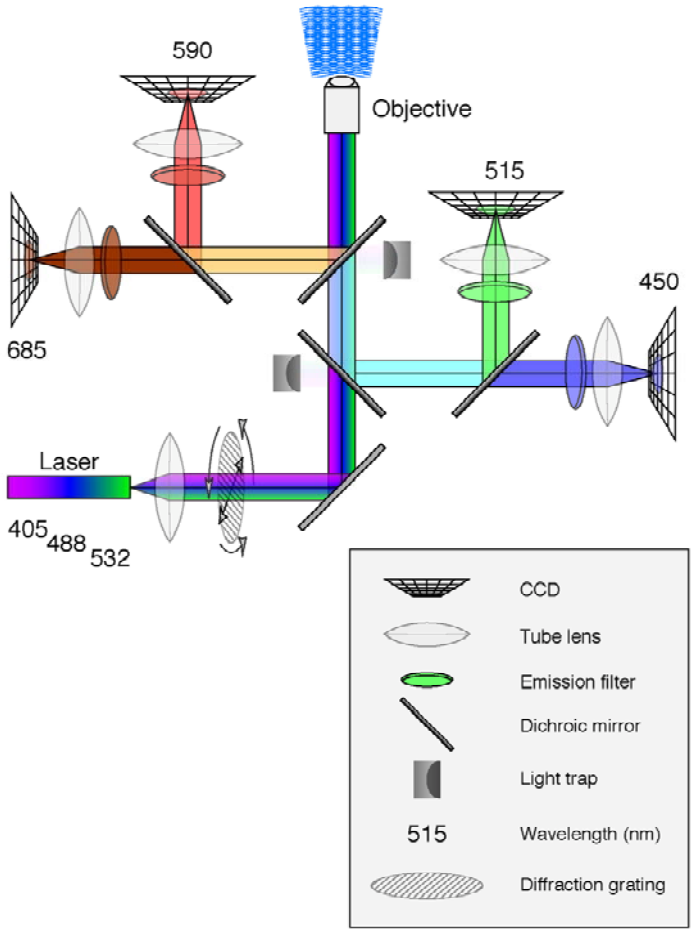

Fig. S6. Schematic of the light path of the OMX microscope. Excitation light from one to three lasers (at 532, 488, or 405 nanometer wavelengths) is transmitted through the set of dichroic mirrors to the objective. Light traps are placed near mirrors transmitting excitation light to prevent reflection of stray light from contaminating the cameras. Emitted fluorescence from the sample returns through the objective and is directed to the proper CCD camera by reflecting from the dichroic mirrors. The mirrors are set into a removable drawer that seats into the microscopy body with kinematic mounting, so that all the mirrors can be replaced as a unit by another pre-aligned set, covering a different selection of wavelength bands, as desired.

Online movies

Movie S1. Three-dimensional view of the nucleus. 3dSIM imaging of nuclear pores (green) and DAPI staining (magenta) in a mouse C2C12 nucleus. The first part shows the slicing through the image stack; the second part shows the rotation of maximum-intensity projections around the x-axis. Scale bar, 5 µm.

Movie S2. 3D volume rendering of a prophase nucleus imaged with 3dSIM, corresponding to Fig. 4. C2C12 cell is immunostained with antibodies against Lamin B and counterstained with DAPI (red). The volume rendering was performed with Volocity 4 software (Improvision).

Supporting references

S1. M. G. Gustafsson *et al., Biophys J*, Epub ahead of print (2008).

S2. Chen, D. D. Hughes, *J Struct Biol* **116**, 56-60 (1996).